

Torque control strategy and optimization for fuel consumption and emission reduction in parallel hybrid electric vehicles

Satoshi Kitayama¹ · Marina Saikyo² · Yui Nishio³ · Kojiro Tsutsumi³

Received: 7 November 2014 / Revised: 9 March 2015 / Accepted: 14 April 2015 / Published online: 4 May 2015
© Springer-Verlag Berlin Heidelberg 2015

Abstract To reduce fuel consumption and exhaust emissions in hybrid electric vehicles (HEVs), it is important to develop a well-organized energy management system (EMS). This paper proposes a torque control strategy coupled with optimization for a parallel HEV. A torque control strategy is developed first. In particular, a function to control the driving condition, called the internal combustion engine (ICE) torque control function, is introduced. This function controls the driving conditions (electric motor (EM) driving, ICE driving, and ICE driving assisted by EM) for reducing fuel consumption and exhaust emissions. This function depends on several design variables that should be optimized. Numerical simulation of HEV using Matlab/Simulink is so computationally intensive that a sequential approximate optimization (SAO) using a radial basis function network (RBF) is adopted to determine the optimal values of these design variables. As the result, the optimal ICE torque control function is determined with a small number of simulation runs. In this paper, CO₂ and NO_x emissions are minimized simultaneously for reducing the fuel consumption and exhaust emission. Through numerical simulations using

typical driving cycles, the trade-off between CO₂ and NO_x emissions is clarified and the validity of the proposed torque control strategy coupled with the proposed optimization is examined.

Keywords Hybrid electric vehicle · Torque control strategy · Multi-objective optimization · Sequential approximate optimization

Abbreviations

BSFC	Brake Specific Fuel Consumption
DOH	Degree of Hybridization
DP	Dynamic Programming
EA	Evolutionary Algorithm
EM	Electric Motor
EMS	Energy Management System
FLC	Fuzzy Logic Control
HEV	Hybrid Electric Vehicle
ICE	Internal Combustion Engine
JC08	Japan Chassis 08
LHD	Latin Hypercube Design
MOO	Multi-Objective Optimization
NEDC	New European Driving Cycle
RBF	Radial Basis Function
SAO	Sequential Approximate Optimization
SOC	State of Charge
WLTC	Worldwide harmonized Light duty driving Test Cycle

✉ Satoshi Kitayama
kitayama-s@se.kanazawa-u.ac.jp

Marina Saikyo
saikyo@stu.kanazawa-u.ac.jp

Yui Nishio
Yui_Nishio@n.t.rd.honda.co.jp

Kojiro Tsutsumi
Kojiro_Tsutsumi@n.t.rd.honda.co.jp

¹ Kanazawa University, Kakuma-machi, Kanazawa 920-1192, Japan

² Graduate School of Natural Science & Technology, Kanazawa University, Kakuma-machi, Kanazawa 920-1192, Japan

³ Honda R&D Co., Ltd. Automobile R&D Center, 4630 Shimotakanezawa Haga-machi Haga-gun, Tochigi 321-3393, Japan

1 Introduction

Zero emission vehicles using electric and fuel cells are an ideal transportation for the environment. Unfortunately, both the

battery and the fuel cell technologies are currently under development. Therefore, hybrid electric vehicles (HEVs) using both an internal combustion engine (ICE) and electric motor(s) (EM) are an alternative for reducing fuel consumption and exhaust emissions. Hybrid technology is one of the most promising research areas recently, and automotive industries are trying to develop several new hybrid technologies for the environment. To reduce the exhaust emissions as well as the fuel consumption, it is important to develop and optimize not only the architecture and components of HEVs, but also the energy management system (EMS), for controlling the energy flow among the components.

There are many hybrid types in HEVs, among which series and parallel HEVs are the typical systems. In this paper, a parallel HEV with a diesel engine is discussed. Figure 1 illustrates the block diagram schematic of the parallel HEV configuration, in which the torque (or power) is provided from both the diesel engine and the electric motor. The propulsion power is transferred to the wheel via the transmission. While braking, the kinetic energy can be converted into electrical energy that is transferred to the electrical storage system. In this paper, CO₂ and NO_x are minimized simultaneously. CO₂ emission is closely related to fuel consumption, whereas NO_x is one of the representative exhaust emissions in the HEV with a diesel engine.

In addition, we assume that the HEV will not be EM-dominated, but ICE-dominated. Therefore, the ICE provides the main propulsion power, and the EM assists it. In this case, the following driving conditions should be taken into account for reducing CO₂ and NO_x emissions: (1) driving only using the EM (EM driving), (2) driving only using the ICE (ICE driving), and (3) driving using both the ICE and EM (ICE driving assisted by EM). The following issues are generally important for CO₂ and NO_x emissions reduction:

- (1) Develop a well-organized EMS considering the above three driving conditions, and
- (2) Operate the ICE on the optimal torque curve on the efficiency map (Chau and Wong 2002).

In particular, the torque distribution between the ICE and the EM is one of the important issues, and many papers have been published on the EMS. Here, the following approaches

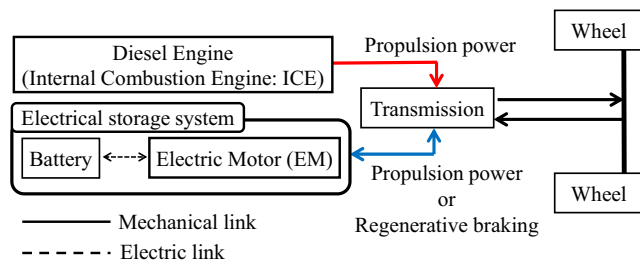


Fig. 1 Block diagram of a parallel HEV system

are mainly discussed: (1) the fuzzy logic control (FLC) including the rule-based approach, (2) the dynamic programming (DP), and (3) the evolutionary algorithms (EAs). In the following section, we briefly review some of these approaches.

Early work on the FLC can be found in Ref. (Baumann et al. 2000), in which the 25-rules fuzzy controller was developed by using the fuzzy sets of the EM torque and the battery state of charge (SOC). In particular, a new concept called the degree of hybridization (DOH) was proposed. This DOH provides a quantitative measure of where power is flowing in a hybrid. Schouten et al. proposed a fuzzy logic controller using the driver power, the battery SOC, and the EM speed for reducing the fuel consumption (Schouten et al. 2003). Kheir et al. developed a generalized fuzzy logic controller based on Ref. (Schouten et al. 2003), in which 44 rules were introduced (Kheir et al. 2004). Unlike Ref. (Schouten et al. 2003), this paper aimed to optimize not only the fuel consumption but also NO_x emission. The trade-off between fuel consumption and NO_x emission was then discussed. Hui et al. developed a fuzzy torque control strategy based on the vehicle load changes (Hui et al. 2009), in which the difference between the optimal torque and the vehicle required torque, the battery SOC, and the vehicle load were used as the fuzzy set. Another rule-based approach can be found in Ref. (Zhu et al. 2006), in which the optimal power distribution considering torque was discussed. The FLC approach is easy to implement and may be suitable for real-time control, but the rules and the fuzzy sets are determined based on the designer's experience and intuition. In addition, the rules are not always optimized in accordance to the driving condition.

The DP approach is widely used in the EMS optimization of HEVs, and many studies have already been reported. The approach using the DP is so similar that only a few papers are reviewed herein. Lin et al. clarified several advantages of the DP, compared to the rule-based approach (Lin et al. 2003). In their work, the ICE speed, the ICE torque, and the EM torque were considered under the delta SOC constraint. In addition, NO_x emission and PM as well as the fuel consumption were all taken into account. The optimal control problem was also formulated and the DP approach was applied to estimate the optimal ICE and EM torque and ICE speed. Perez et al. determined the optimal power flow between the ICE and the EM so as to minimize the fuel consumption (Perez et al. 2006). Pei and Leamy computed the optimal ICE/EM torque, the ICE/EM speed and gear using the DP (Pei and Leamy 2013). A similar approach can also be found in Ref. (Kum et al. 2011). In addition, a comparison between the DP and the FLC has been conducted in Ref. (Guemri et al. 2014). Nevertheless, the DP has the following advantages, compared to the FLC:

- (A1) It can handle more than two objectives (Koot and Kesseks 2005; Wang et al. 2012). Most of papers adopt the weighted sum. In other words, multi-objective

optimization is transformed into one objective function with the weighted sum.

- (A2) It can easily handle the delta SOC that is given by the difference between the initial and the final SOC, where the initial SOC implies the battery SOC at the beginning of a driving cycle and the final SOC the battery SOC at the end of a driving cycle. It is preferable that the delta SOC will be zero for energy management consideration. Thus, the delta SOC plays an important role in the development of the EMS algorithm. Since the delta SOC is a design constraint (requirement), it is then handled as a penalty function (Sinoquet et al. 2011).

In contrast to the above advantages, the DP also has the following disadvantages:

- (D1) The weighted sum has several disadvantages (Miettinen 1998). To overcome or avoid these disadvantages, another method should be adopted.
- (D2) The DP approach is basically optimal control (Delprat et al. 2004). To find optimal control law, a high computational cost is required.

Recently, the approach using the EAs such as the genetic algorithm (GA) and the particle swarm optimization (PSO) has received much attention. Montazeri-Gh et al. applied the GA to HEV control strategy (Montazeri-Gh et al. 2006), in which four objectives (CO_2 , HC, CO, and NO_x) were taken into account. As described above, the weighted sum was adopted to handle these objectives. Various weights were assigned and the trade-off among them was investigated. The PSO was also applied to the HEV powertrain (Wu et al. 2008), in which the weighted sum was adopted to handle five objectives (CO_2 , HC, CO, NO_x , and cost). A simple control strategy was constructed, and the PSO was used to determine the parameters in the control strategy. The application of EAs to the EMS optimization was valid, but this approach generally required a large number of simulation runs. In addition, the delta SOC was rarely discussed (Wu et al. 2008; Long and Nhan 2012).

These representative approaches directly calculate the fuel consumption and emissions, but the simulation in HEV is computationally intensive. In addition, many papers employ the optimal torque curve on the engine efficiency map, but this is dependent on the designer's experience and intuition. When it is difficult to determine and identify the optimal torque curve, another approach for CO_2 and NO_x emissions reduction is to refer to the brake specific fuel consumption (BSFC) map. In this paper, we propose a torque control strategy coupled with optimization for CO_2 and NO_x emissions reduction referring to the BSFC map. The summary of this paper is described below:

- (1) First, a torque control strategy aiming to minimize CO_2 and NO_x emissions is developed. In particular, the ICE torque control function explained in section 3 is introduced. This function controls the driving condition for both the CO_2 and NO_x emissions reduction.
- (2) The ICE torque control function depends on several design variables. To determine this function, optimization is performed. Unfortunately, the simulation in HEV is so computationally intensive that it is preferable to determine this function with a small number of simulation runs. Under this situation, the response surface approach is valid. In particular, a sequential approximate optimization (SAO) that the response surface is repeatedly constructed and optimized is one of the powerful tools available. The Kriging is a famous SAO approach (Donald et al. 1998), and we have developed the SAO system using a radial basis function (RBF) network (Kitayama et al. 2011; Kitayma et al. 2013). By using this SAO system, the ICE torque control function is determined.

The driving cycle is generally unknown in advance. Fortunately, several typical driving cycles, such as the New European Driving Cycle (NEDC), are widely used as the benchmarks for testing the EMS optimization. Three representative driving cycles are then used to examine the validity of the proposed torque control strategy coupled with the optimization.

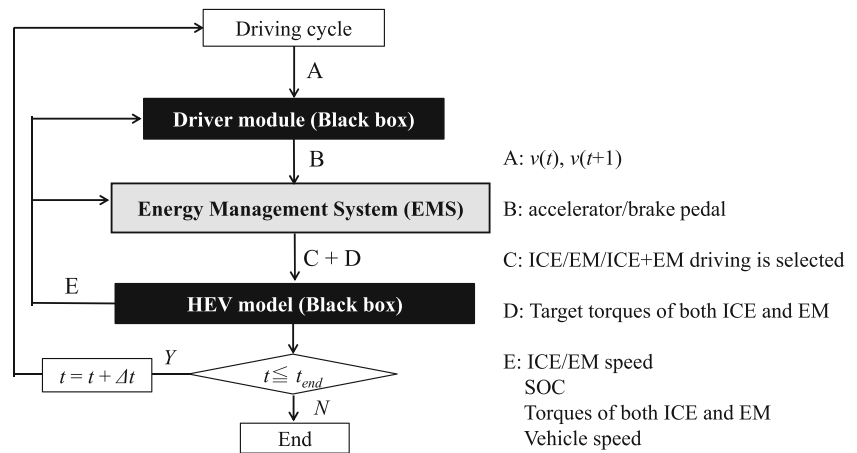
This paper is organized as follows: In section 2, the HEV simulation model is described. In section 3, the proposed torque control strategy is described. Numerical results are shown, the pareto-frontier is identified, and the validity of the proposed approach is discussed. Matlab/Simulink is used in all the HEV numerical simulations.

2 Flow of HEV simulation

Figure 2 shows the flow of the HEV simulation in which two black boxes are included. The flow of the simulation proceeds as follows:

At first, the vehicle speeds $v(t)$ and $v(t+1)$ are obtained from the driving cycle block at time t , and their values are then sent to the driver model module. The accelerator/brake pedal is then calculated in the driver model module, and the solutions are sent to the EMS module. In the EMS module, a single driving condition among the EM driving, ICE driving, and ICE driving assisted by EM is first selected. In addition, the target torque values for both the ICE and the EM are determined. These values are then sent to the HEV model module, where the ICE/EM speed, the battery SOC, the torque values for both the ICE and the EM, and the vehicle speed are calculated. These are fed back to both the driver model module and the EMS module. CO_2 and NO_x at time t are

Fig. 2 Flow of the HEV simulation



calculated in the HEV model module, and the sum of them at time t_{end} is considered as the objective functions. To reduce CO_2 and NO_x emissions, we can arrange the EMS module highlighted in gray in Fig. 2. A c-segment car with 7-speed AMT is assumed as the HEV. Note that in this paper the battery is not charged by the diesel engine and is charged only by the regenerative braking through a driving cycle.

To reduce CO_2 and NO_x emissions, the ICE/EM speed and gear should also be taken into account. Unfortunately, these latter two parameters are included in the black boxes and we cannot change them.

3 Torque control strategy for determining the ICE torque control function

As described in Ref. (Chau and Wong 2002), the ICE operation along with the optimal torque curve directly affects the exhaust emissions as well as the fuel consumption. In this paper, the ICE torque control function that controls the driving conditions is introduced for CO_2 and NO_x emissions reduction. Seven design variables are included in this function, and these are determined by the SAO using the RBF network.

3.1 Torque control strategy

The proposed torque control strategy is shown in Fig. 3, where “ICE” implies the ICE driving, “EM” the EM driving, and “ICE+EM” the ICE driving assisted by the EM. Note that the EMS module in Fig. 3 is replaced with that in Fig. 2. Figure 4 shows the basic driving conditions based on BSFC map with the ICE torque control function. It is clear from Fig. 4 that the three driving conditions (EM driving, ICE driving, and ICE driving assisted by EM) are taken into account for CO_2 and NO_x emissions reduction. The illustrative example of the BSFC is shown in Fig. 5, from which it can be found that, in ICE driving only, CO_2 emission reduction is not effective with lower torque and engine speed, whereas NO_x is

produced with higher torque. In other words, the trade-off between CO_2 and NO_x can be found when the ICE driving only is performed. In addition, the EM driving should be performed in the lower torque and engine speed for CO_2 emission reduction, whereas the ICE driving assisted by EM should be performed for NO_x emission reduction. Note that the BSFC map is simply used to refer to CO_2 and NO_x emissions and this map is not used to calculate CO_2 and NO_x emissions. Before explaining the proposed torque control strategy, the following notations are introduced:

SOC_{\min} : Minimum battery SOC determined by the designer. This is not a hard bound of the battery

SOC_{\max} : Maximum battery SOC determined by the designer. This is not a hard bound of the battery

ω_{ICE} : ICE speed

ω_{ICE}^L : Lower bound of the ICE speed

ω_{ICE}^U : Upper bound of the ICE speed

ω_{ICE}^V : ICE speed between ω_{ICE}^L and ω_{ICE}^U

ω_{ICE}^{\max} : Maximum ICE speed

$T_D^{REQ}(t)$: Driving torque request at time t

$T_{ICE}^T(t)$: Target torque of the ICE at time t , which is included in D in Fig. 2

$T_{EM}^T(t)$: Target torque of the EM at time t , which is included in D in Fig. 2

T^{SW} : Switch torque from the EM driving to the ICE driving

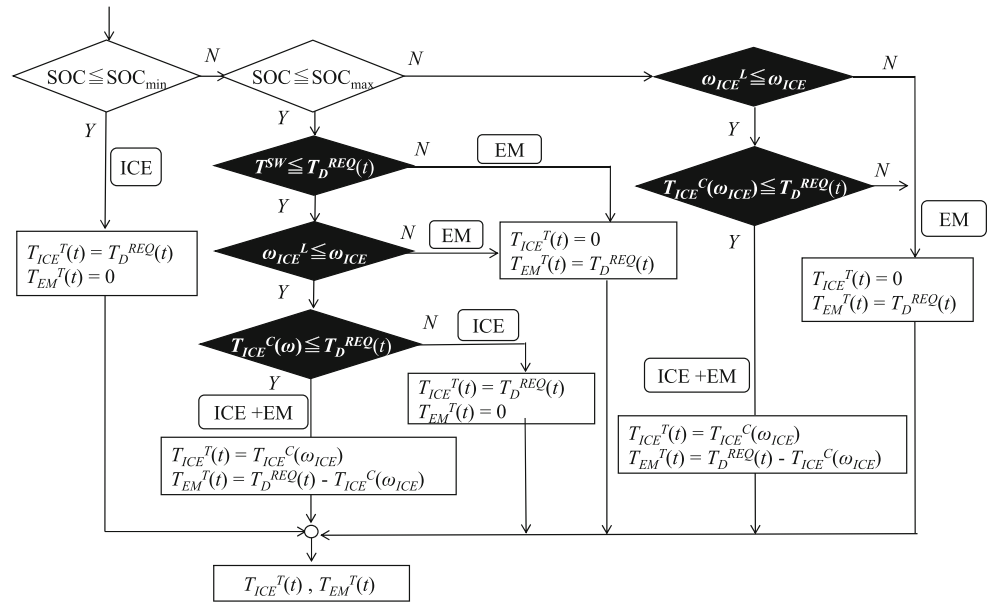
$T_{ICE}^C(\omega_{ICE})$: ICE torque control function

The objective of the proposed torque control strategy is to determine the target torque for both the ICE and the EM at time t ($T_{ICE}^T(t)$ and $T_{EM}^T(t)$).

First, let us explain the left-hand side of Fig. 3. If the battery SOC is less than the SOC_{\min} , the ICE driving is selected. Then, $T_{ICE}^T(t)$ is directly set to $T_D^{REQ}(t)$, and $T_{EM}^T(t)$ is set to zero.

Next, let us explain the right-hand side of Fig. 3. If the battery SOC is greater than the SOC_{\max} , the EM driving or

Fig. 3 Proposed torque control strategy



the ICE driving assisted by EM is selected by considering ω_{ICE} and $T_D^{REQ}(t)$. This situation assumes that the battery will be fully charged. Under this situation, the battery SOC should be actively used to reduce CO₂ and NO_x emissions. The ICE driving region in Fig. 4 is then replaced with the EM driving region as shown in Fig. 6. If ω_{ICE} is less than ω_{ICE}^L , the EM driving is selected (see the area surrounded by the bold line in Fig. 6). Otherwise, $T_D^{REQ}(t)$ is compared to $T_{ICE}^C(\omega_{ICE})$. If $T_D^{REQ}(t)$ is less than $T_{ICE}^C(\omega_{ICE})$, the EM driving is selected as shown in Fig. 6a. Otherwise, the ICE driving assisted by EM is selected as shown in Fig. 6b. $T_{ICE}^T(t)$ is then set to $T_{ICE}^C(\omega_{ICE})$, and the rest of $T_D^{REQ}(t)$ is compensated with $T_{EM}^T(t) (= T_D^{REQ}(t) - T_{ICE}^C(\omega_{ICE}))$.

Finally, let us explain the crucial part of the proposed torque control strategy. This situation assumes that the battery SOC is within the SOC_{min} and SOC_{max}. First, T^{SW} is compared to $T_D^{REQ}(t)$. If $T_D^{REQ}(t)$ is less than T^{SW} , the EM driving is selected. Otherwise, ω_{ICE} is compared to ω_{ICE}^L . If ω_{ICE} is less than ω_{ICE}^L , the EM driving is selected. In the EM driving, $T_{ICE}^T(t)$ is always set to zero, and $T_{EM}^T(t)$ is set to $T_D^{REQ}(t)$. These situations are schematically illustrated in Fig. 7a and b

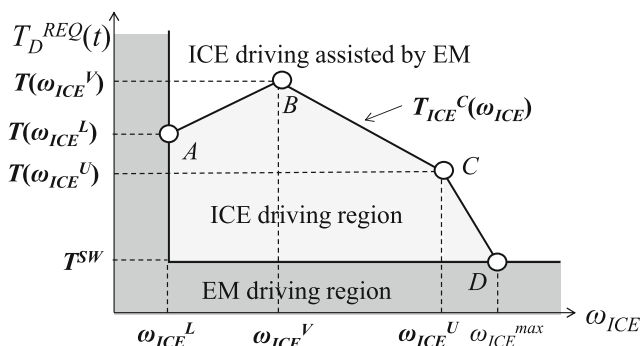


Fig. 4 ICE torque control function and driving conditions

with the bold line. The corresponding torque control strategy proposed is shown in Fig. 7c.

Next, the ICE driving or the ICE driving assisted by EM is selected, by comparing $T_{ICE}^C(\omega_{ICE})$ and $T_D^{REQ}(t)$. The schematic example and the corresponding torque control strategy flow diagram are shown in Fig. 8, where we consider the area surrounded by the bold line. If $T_{ICE}^C(\omega_{ICE})$ is less than $T_D^{REQ}(t)$, the ICE driving assisted by EM is selected. In this case, $T_{ICE}^T(t)$ is set to $T_D^{REQ}(t)$ and the rest of $T_D^{REQ}(t)$ is compensated with $T_{EM}^T(t) (= T_D^{REQ}(t) - T_{ICE}^C(\omega_{ICE}))$. Otherwise, the ICE driving is selected, and $T_{ICE}^T(t)$ is directly set to $T_D^{REQ}(t)$.

Several characteristics of the proposed torque control strategy are summarized as follows:

1. Unlike the FLC and DP approaches (Schouten et al. 2003; Kheir et al. 2004; Hui et al. 2009; Lin et al. 2003), the ICE torque control function referring to the BSFC map is introduced for CO₂ and NO_x emissions reduction. In

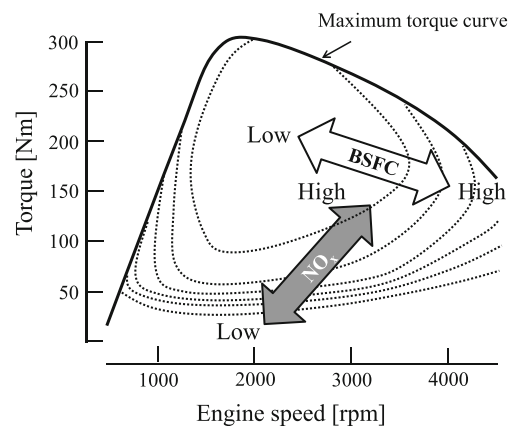
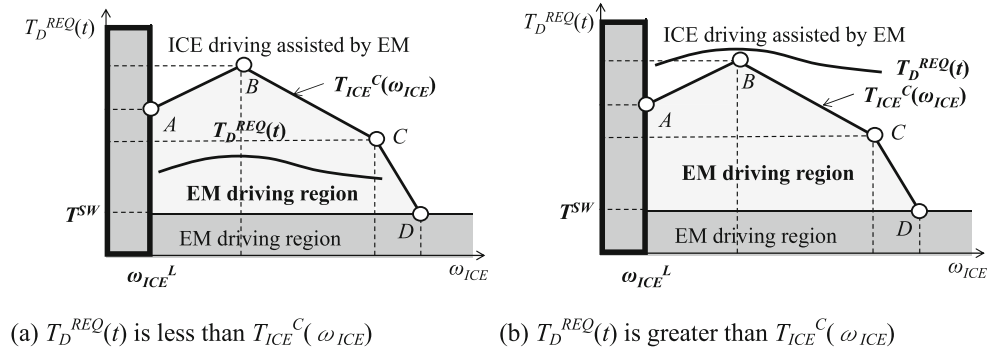


Fig. 5 Illustrative example of the BSFC map on torque-engine speed plane

Fig. 6 ICE torque-speed plane in the case of SOC_{max} is less than SOC. **a** $T_D^{REQ}(t)$ is less than $T_{ICE}^C(\omega_{ICE})$ **b** $T_D^{REQ}(t)$ is greater than $T_{ICE}^C(\omega_{ICE})$



- particular, this function controls the three driving conditions. In addition, this function can take into account the nonlinearity of CO₂ and NO_x emissions reduction.
2. A constant torque curve has been assumed in previous papers (Montazeri-Gh et al. 2006; Wu et al. 2008; Long and Nhan 2012). In contrast to such papers, the proposed approach can take into account the nonlinear torque request curve for practical applications.
 3. By introducing ω_{ICE} , the EM driving is taken into account for the lower range of the engine speed for CO₂ emission reduction.
 4. When the battery is fully charged, the ICE driving region is replaced by the EM driving. Therefore, the proposed torque control strategy is designed to use the battery SOC actively. As the result, it is expected that the battery SOC is effectively used to reduce CO₂ and NO_x emissions.

3.2 Design variables

As shown in Fig. 4, four points (A, B, C, and D) are used to determine the ICE torque control function. At point D, ω_{ICE}^{max} is practically regarded to be constant. In this paper,

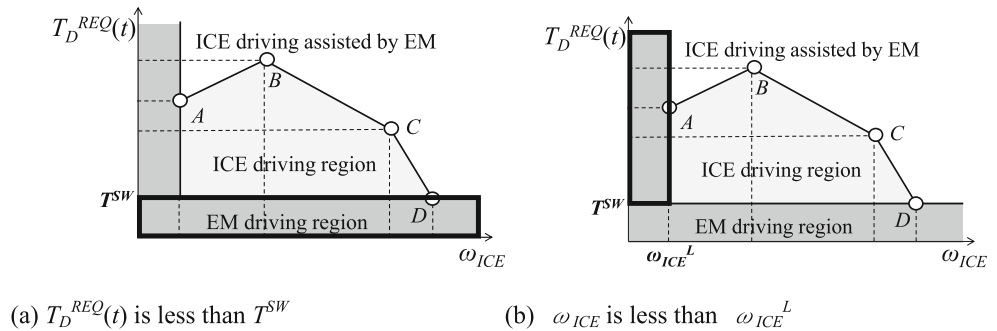
ω_{ICE}^{max} is taken as the engine speed of the red-zone ($\omega_{ICE}^{max} = 4500$ rpm). In addition, T^{SW} is introduced to denote the switch torque from the EM driving to the ICE driving. As the result, the ICE torque control function consists of seven design variables ($\omega_{ICE}^L, \omega_{ICE}^V, \omega_{ICE}^U, T^{SW}, T(\omega_{ICE}^L), T(\omega_{ICE}^V),$ and $T(\omega_{ICE}^U)$).

3.3 Sequential approximate optimization

In this paper, CO₂ and NO_x are minimized simultaneously. Thus, the problem is formulated as a multi-objective optimization (MOO). To determine these design variables, the SAO using RBF network is used. Here, the flow to determine the ICE torque control function is described.

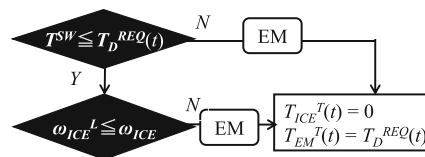
- (STEP1) Some initial sampling points are generated by the latin hypercube design (LHD).
- (STEP2) Numerical simulation is carried out. Objective functions (CO₂ and NO_x) are numerically evaluated at all sampling points.
- (STEP3) All functions are approximated by the RBF network. Here, the approximated objective functions are denoted as $\tilde{f}_i(\mathbf{x})$ ($i=1,2,\dots,K$).

Fig. 7 Conditions of the EM driving. **a** $T_D^{REQ}(t)$ is less than T^{SW} **b** ω_{ICE} is less than ω_{ICE}^L (c) Corresponding torque control strategy of the EMS algorithm



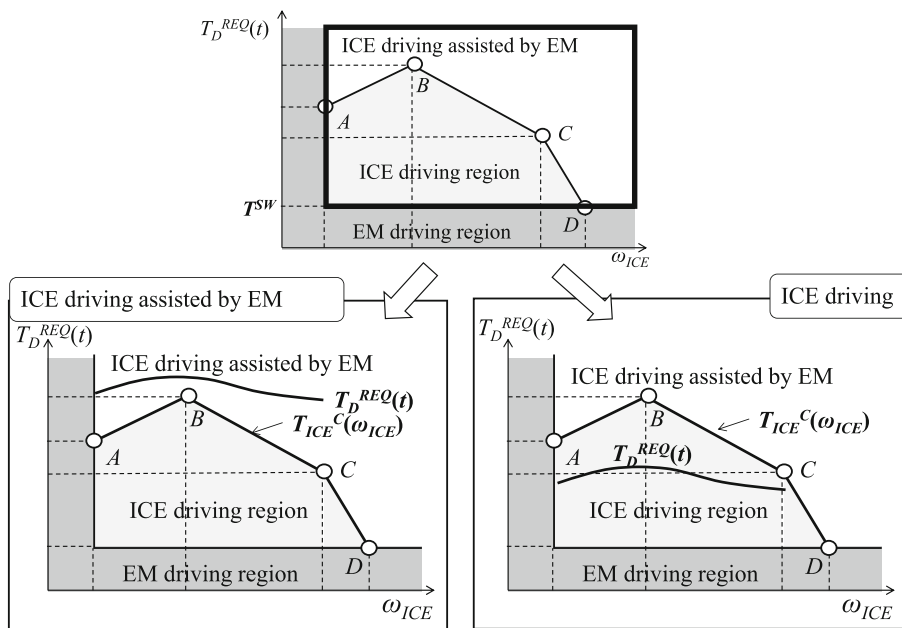
(a) $T_D^{REQ}(t)$ is less than T^{SW}

(b) ω_{ICE} is less than ω_{ICE}^L

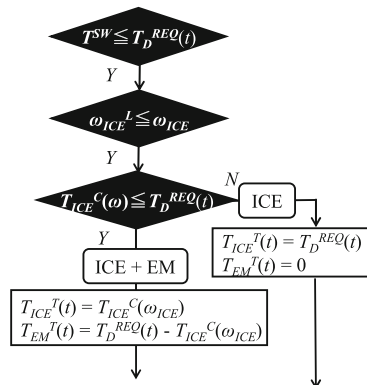


(c) Corresponding torque control strategy of the EMS algorithm

Fig. 8 Conditions of the ICE driving/ICE driving assisted by EM. **a** ICE driving assisted by EM/ ICE driving **b** Corresponding torque control strategy of the EMS algorithm



(a) ICE driving assisted by EM/ ICE driving



(b) Corresponding torque control strategy of the EMS algorithm

(STEP4) We find a pareto-optimal solution of response surface with the weighted l_p norm method formulated as follows (Miettinen 1998):

$$\left[\sum_{i=1}^K (\alpha_i \tilde{f}_i(\mathbf{x}))^p \right]^{1/p} \rightarrow \min \quad (1)$$

where α_i ($i=1,2,\dots,K$) represents the weight of the i -th objective function, and p is the parameter. In this paper, p is set to 4. In order to obtain a set of pareto-optimal solutions, various weights are assigned.

(STEP5) The density function is constructed and minimized. The optimal solution of the density function is added as a new sampling point. This step is repeated till a terminal criterion is satisfied.

(STEP6) If terminal criterion is satisfied, the SAO algorithm will be terminated. Otherwise, it will return to STEP 2.

The differential evolution (DE) is used as the optimizer in STEPS 4 and 5. There are various models in the DE, and the most basic model (DE/rand/1/bin) is used. The DE has several parameters such as the number of populations, the maximum search iteration number, the mutation ratio, and the crossover ratio. Through numerical experiences, the following parameters are used: the number of populations 50, the maximum search iteration number 1000, the mutation ratio 0.8, the crossover ratio 0.5.

4 Numerical result and discussion

4.1 Driving cycle and pareto-frontier

Through numerical simulation, the validity of the proposed approach is examined. SOC_{\min} and SOC_{\max} are set to 45 %

and 65 %, respectively. In this paper, the following representative driving cycles are used:

- (1) New European Driving Cycle (NEDC): This consists of four identical urban cycles and one extra-urban cycle. This is one of the widely used benchmarks for testing EMS.
- (2) Japan Chassis 08 (JC08): This is the driving cycle regulated by the Ministry of Land, Infrastructure, Transport and Tourism in Japan. Ordinary and compact cars are required to report the fuel consumption. The average vehicle speed of this driving cycle is 24.4 km/h, and urban driving is mainly assumed.
- (3) Worldwide harmonized Light duty driving Test Cycle (WLTC): This cycle consists of the following four speed ranges: (1) Low (589 s), (2) Middle (433 s), (3) High (455 s), and Extra-high (323 s). Unlike other cycles, this cycle includes the extra-high speed range where the maximum speed is 131.3 km/h. It is expected that NO_x emission will increase in this range. As a result, this cycle is one of the challenging driving cycles for CO₂ and NO_x emissions reduction.

These three driving cycles are shown in Fig. 9(a)~(c). In addition, the cycle time, the average and maximum speed, and the driving distances are listed in Table 1.

To identify the pareto-frontier, eighteen initial sampling points are distributed by the LHD. The error between the response surface and the numerical simulation is taken as the terminal criterion with the error set to 1.0 %. Therefore, the SAO algorithm will be terminated when the error is within 1 %. The lower and upper bounds of the design variables in each driving cycle are set as follow:

For NEDC:

$$\begin{aligned} 800 \leq \omega_{ICE}^L \leq 1500 \quad 1500 \leq \omega_{ICE}^V \leq 2500 \quad 2500 \leq \omega_{ICE}^U \leq 3500 \\ 25 \leq T^{SW} \leq 70 \quad 70 \leq T(\omega_{ICE}^L), T(\omega_{ICE}^V), T(\omega_{ICE}^U) \leq 150 \end{aligned} \quad (2)$$

For JC08:

$$\begin{aligned} 800 \leq \omega_{ICE}^L \leq 1500 \quad 1500 \leq \omega_{ICE}^V \leq 2500 \quad 2500 \leq \omega_{ICE}^U \leq 3500 \\ 20 \leq T^{SW} \leq 35 \quad 50 \leq T(\omega_{ICE}^L), T(\omega_{ICE}^V), T(\omega_{ICE}^U) \leq 100 \end{aligned} \quad (3)$$

For WLTC:

$$\begin{aligned} 800 \leq \omega_{ICE}^L \leq 1500 \quad 1500 \leq \omega_{ICE}^V \leq 2500 \quad 2500 \leq \omega_{ICE}^U \leq 3500 \\ 25 \leq T^{SW} \leq 60 \quad 70 \leq T(\omega_{ICE}^L), T(\omega_{ICE}^V), T(\omega_{ICE}^U) \leq 140 \end{aligned} \quad (4)$$

Figure 10a-c shows the pareto-frontier of each driving cycle, where the white dots denote the sampling points and the black dots the points on the pareto-frontier of the response

surface using the sampling points. Here, we would like to explain the pareto-frontier of WLTC. Several white dots can be found below the black dots, and these may be considered as the pareto-optimal solutions. Various weights are assigned to identify the pareto-frontier, but we never obtained these white dots and always obtained the black dots. Then, we considered the black dots represent the pareto-frontier. In addition, we confirmed that all numerical simulation results showed that a final SOC equals to the initial one. Therefore, the delta SOC is zero at all points. The right hand side of Fig. 10 shows the enlarged view around the pareto-frontier. It can be found from Fig. 10 that the pareto-frontier of both NEDC and JC08 is continuous, whereas the pareto-frontier of WLTC is discontinuous. In order to identify the pareto-frontier, 36 simulation runs were required in NEDC, 67 simulation runs in JC08, and 63 simulation runs in WLTC.

4.2 Battery SOC variation and ICE operating points

It is found from Fig. 10 that the pareto-frontier is continuous and that the variation of CO₂ and NO_x emissions is small in the cases of NEDC and JC08, whereas the pareto-frontier of WLTC is discontinuous. In the case of WLTC, the variation of CO₂ and NO_x emissions in the regions enclosed by two circles is quite small. Based on these findings, we considered that it would be still possible to compare WLTC's operating characteristics for these two regions. The representative point indicated by the arrows in Fig. 10 (NEDC-A, JC08-A, WLTC-A, and WLTC-B) is then selected for the discussion. Specifically, the following points are included in Figs. 11, 12, and 13, for the analysis and the discussion:

- (a) The battery SOC variation through the driving cycle
- (b) The time history of the ICE torque and the value of the ICE torque control function
- (c) The ICE operating points denoted by the cross mark, plotted at the intervals of 1 s. In order to perform the ICE driving and the ICE driving assisted by EM, the ICE inevitably overlaps through the EM driving region. As a result, the ICE operating points are plotted in the EM driving region. In addition, as explained in section 3.1, all ICE operating points ideally lie on and under the ICE torque control function for CO₂ and NO_x emissions reduction. If the ICE operating points are plotted above the ICE control function, this implies that ICE driving should be performed, due to the lack of a total torque request. Unfortunately, NO_x emission will increase in the ICE driving assisted by EM. Finally, the ICE operating points plotted on the ICE torque control function implies the use of the ICE driving assisted by EM.
- (d) The time history of torque between ICE and EM. This figure shows the torque distribution through the driving

Fig. 9 Representative driving cycles

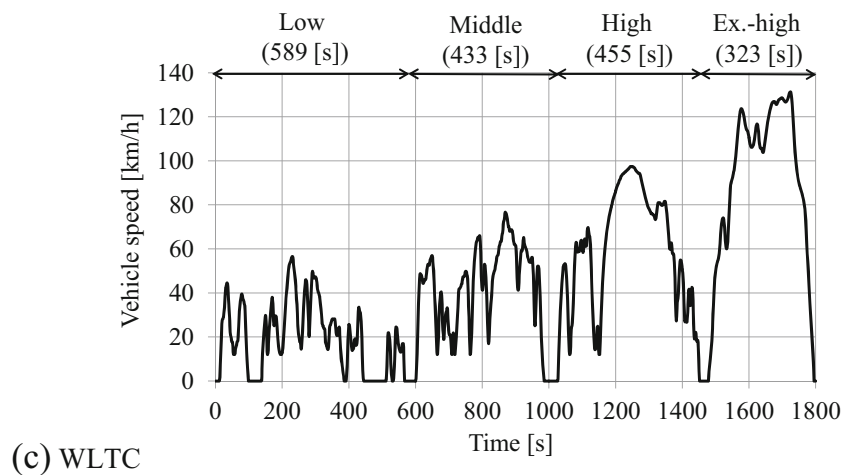
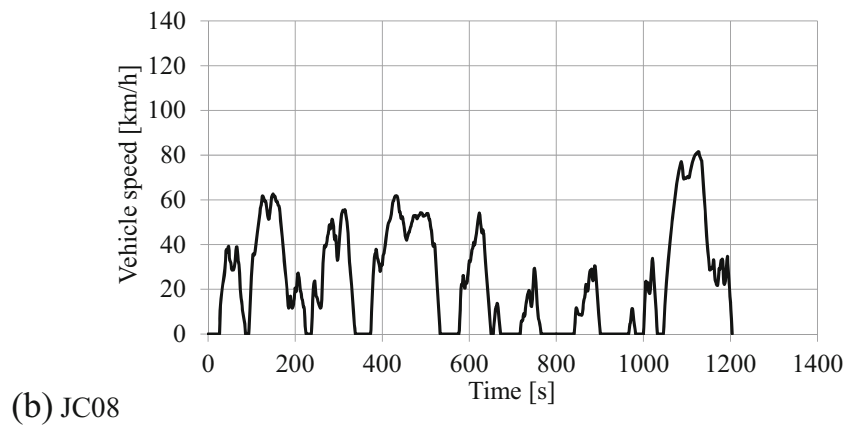
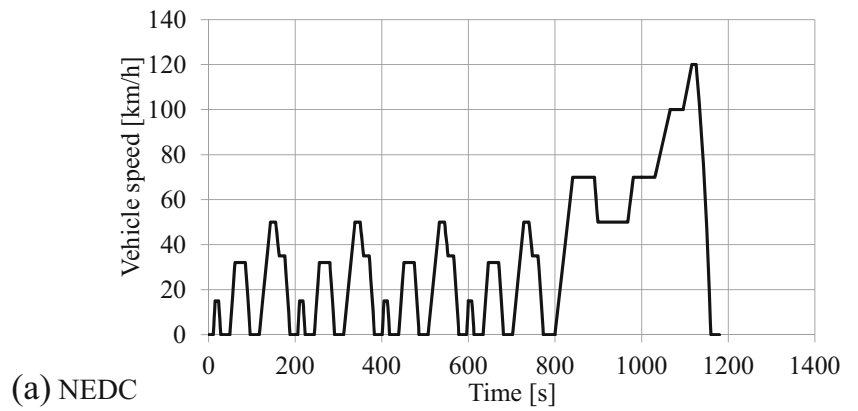
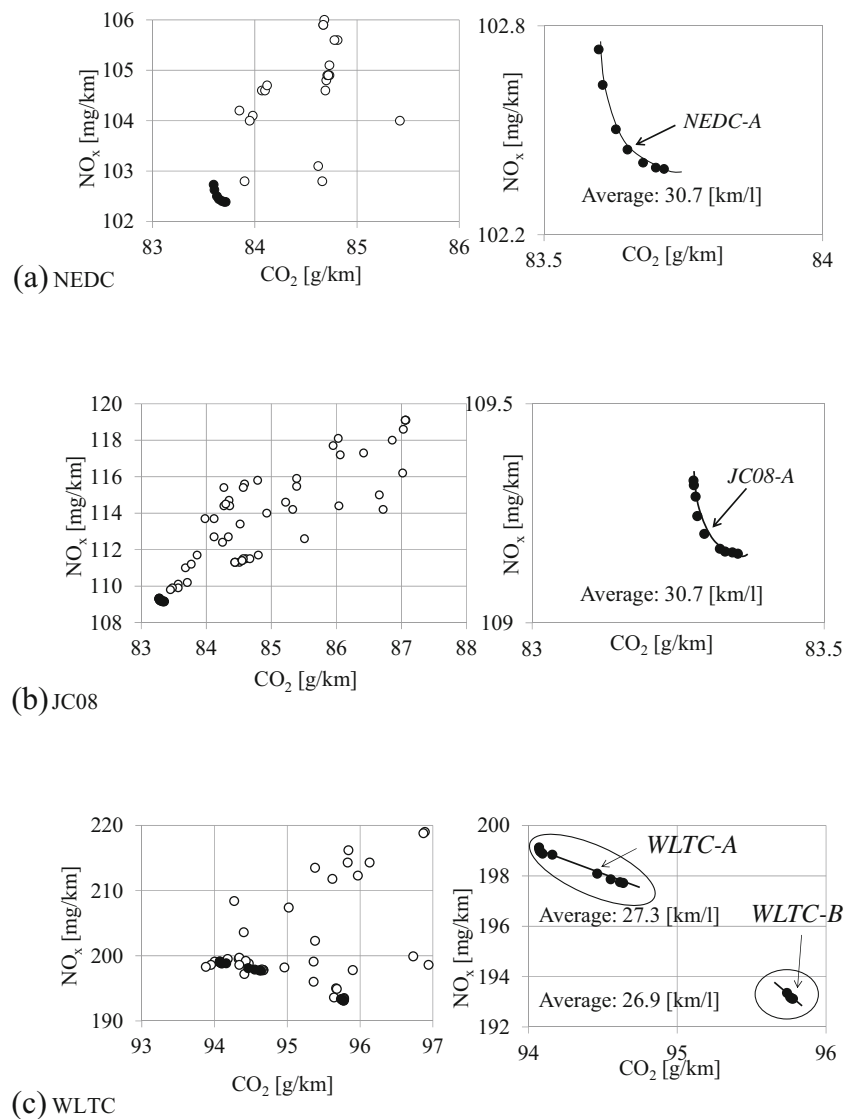


Table 1 Outline of the NEDC/JC08/WLTC driving cycle characteristics

Driving Cycle	Cycle Time [s]	Average speed [km/h]	Maximum speed [km/h]	Driving Distance [km]
NEDC	1180	33.6	120	11.01
JC08	1204	24.4	81.6	8.17
WLTC	1800	46.5	131.3	23.17

Fig. 10 Pareto-frontier of each driving cycle



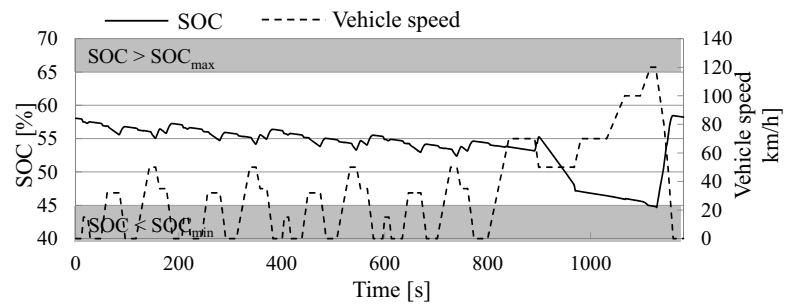
cycle. In this figure, it can be identified when the EM/ICE/ICE+EM driving condition is selected. In the same figure, the black line denotes the ICE driving condition and the red line the EM driving condition. It is impossible to show all the parts of the ICE driving assisted by EM and so, only the major part of this driving condition is indicated, enclosed by a circle.

First, let us consider NEDC driving cycle. It is found from Fig. 11a that the battery SOC through the driving cycle is within the SOC_{min} and SOC_{max} . It is also found from Fig. 11b that most of the ICE torque values are less than the values of the ICE torque control function during the driving cycle. Many ICE operating points are then plotted below the ICE torque control function, as shown in Fig. 11c. However, the ICE torque is greater than the value of ICE torque function around the region enclosed by the circle in Fig. 11b. The ICE operating points are then

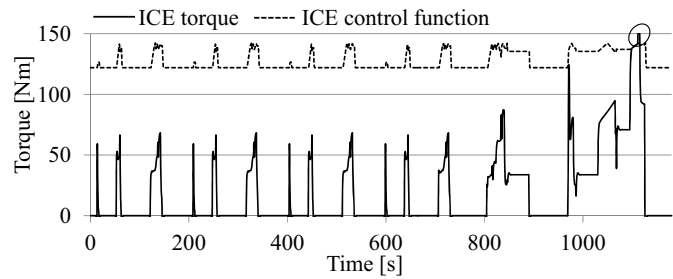
plotted above the ICE torque control function, as shown in Fig. 11c. Finally the ICE operating points on the ICE torque control function implies the ICE driving assisted by EM for NO_x emission reduction. It is found from Fig. 11c and d that the EM and ICE driving are primarily performed at NEDC-A.

Next, JC08 driving cycle is considered. The battery SOC through the driving cycle is within the SOC_{min} and SOC_{max} , like NEDC driving cycle. However, as shown in Fig. 12c, numerous ICE operating points are plotted on the ICE torque control function, in comparison with NEDC driving cycle. This implies that the ICE driving assisted by EM is more often performed in this case, in comparison with NEDC driving cycle. In addition, all ICE operating points lie on and under the torque control function. Therefore, the proposed torque control strategy coupled with the optimization works well for CO_2 and NO_x emissions reduction.

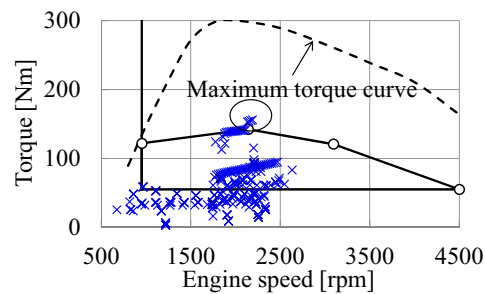
Fig. 11 Battery SOC variation and ICE operating points in the NEDC driving cycle at NEDC-A. **a** Battery SOC variation through the driving cycle **b** Time history of the ICE torque and the value of the ICE torque control function **c** ICE operating points **d** Time history of torque between the ICE and the EM driving conditions



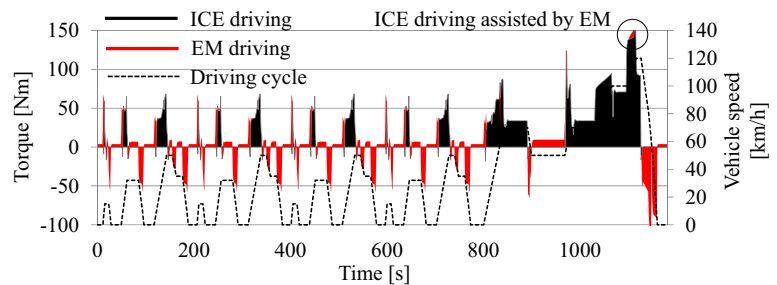
(a) Battery SOC variation through the driving cycle



(b) Time history of the ICE torque and the value of the ICE torque control function



(c) ICE operating points

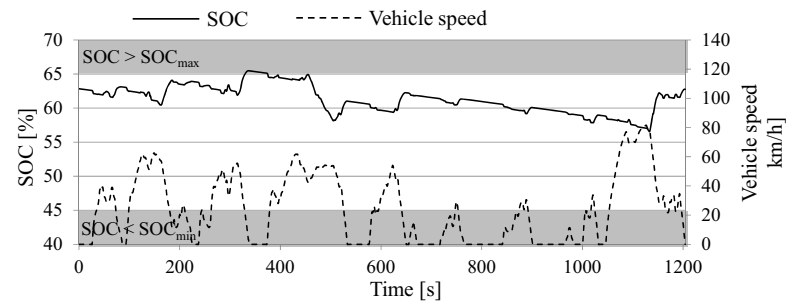


(d) Time history of torque between the ICE and the EM driving conditions

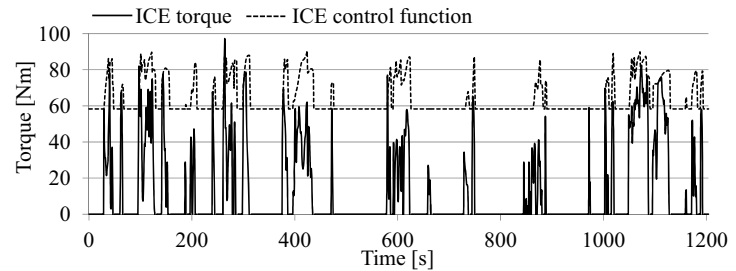
Finally, WLTC driving cycle is discussed. Since the pareto-frontier is discontinuous, the characteristics at WLTC-A and WLTC-B are discussed respectively. The solid line in Fig. 13a represents the variation of battery SOC at WLTC-A in Fig. 10c, and the dashed line the variation of SOC at WLTC-B in Fig. 10c. Unlike NEDC-A and JC08-A, the battery SOC is sometimes over the SOC_{max} . In this case, as also shown in Fig. 6, the EM driving or the ICE driving assisted by EM is selected. Since the WLTC driving

cycle includes the extra-high speed range, the battery SOC is actively used for CO_2 and NO_x emissions reduction in this range. It is found from Fig. 13a that the battery SOC is well charged by the regenerative braking in the low, middle, and high speed ranges and is only actively used in the extra-high speed range. In addition, it is found from Fig. 13c and d that the ICE driving assisted by EM is often performed at the WLTC-A and WLTC-B. However, at WLTC-B, more ICE operating points are plotted above

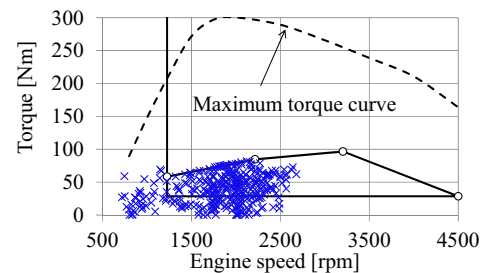
Fig. 12 Battery SOC variation and ICE operating points in the JC08 driving cycle at JC08-A. **a** Battery SOC variation through the driving cycle **b** Time history of the ICE torque and the value of the ICE torque control function **c** ICE operating points **d** Time history of torque between the ICE and the EM driving conditions



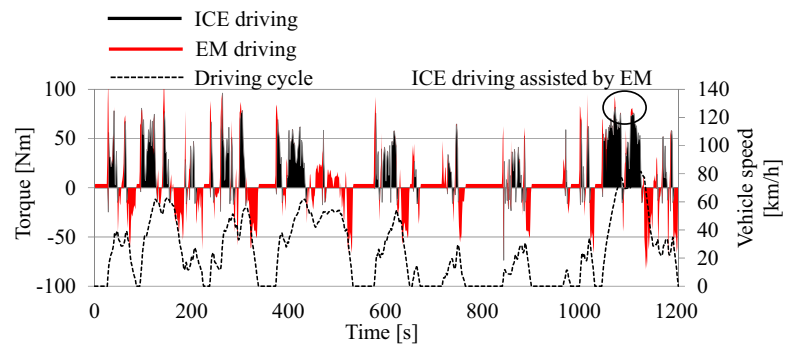
(a) Battery SOC variation through the driving cycle



(b) Time history of the ICE torque and the value of the ICE torque control function



(c) ICE operating points

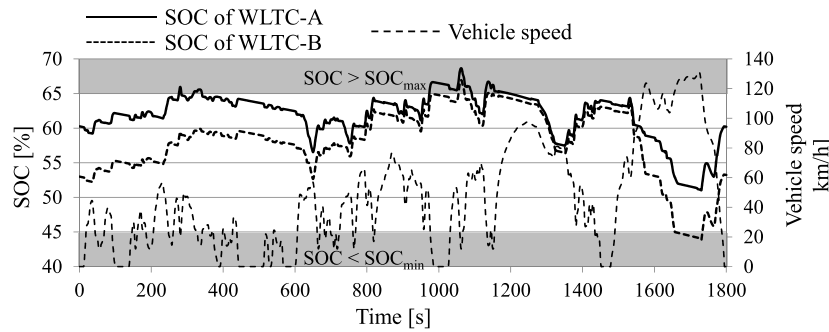


(d) Time history of torque between the ICE and the EM driving conditions

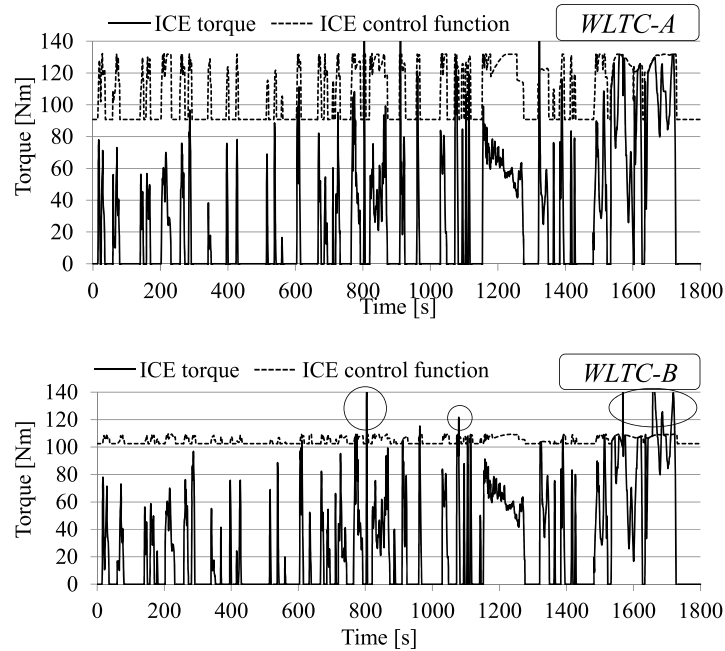
the ICE torque control function. This can be understood from Fig. 13b that the ICE torque is greater than the value of ICE torque function around the regions enclosed by the circles. On the other hand, it is found from Fig. 13c that all ICE operating points lie on and under the ICE torque control function at WLTC-A. Therefore, we can infer that the proposed torque control strategy coupled with the

optimization works well at this point. However, the trade-off can be observed between CO_2 and NO_x emissions, and it is difficult to conclude which point is better.

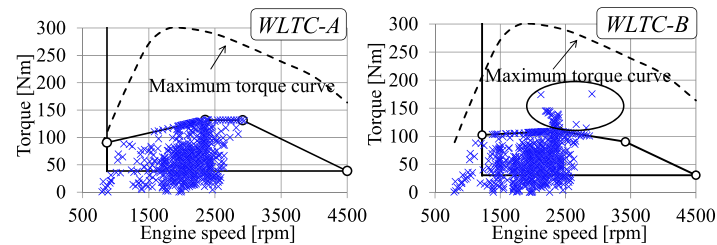
With all things considered, the proposed torque control strategy coupled with optimization leads to a well-organized EMS system and to effective reductions in CO_2 and NO_x emissions.



(a) Battery SOC variation through the driving cycle



(b) Time history of the ICE torque and the value of the ICE torque control function



(c) ICE operating points

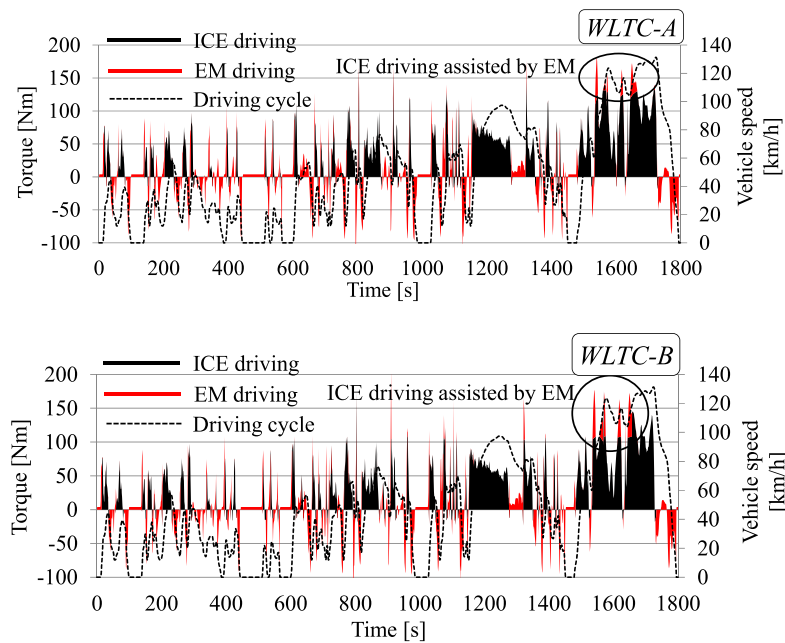
Fig. 13 Battery SOC variation and ICE operating points in the WLTC driving cycle at WLTC-A and WLTC-B in Fig. 10c. **a** Battery SOC variation through the driving cycle **b** Time history of the ICE torque

and the value of the ICE torque control function **c** ICE operating points **d** Time history of torque between the ICE and the EM driving conditions

4.3 Improvement of CO₂ and NO_x

There are various HEVs such as a series, a parallel, and their mixed HEVs, and the engine and the transmission types are also different (gasoline or diesel engine, AT or CVT). Therefore, it is difficult to simply compare CO₂ and NO_x emissions

reduction under same conditions. Then, CO₂ and NO_x emissions reduction are compared to the ICE driving only by using this HEV model. Therefore, the ICE driving is performed in the torque-engine speed plane. The summary of comparison is listed in Table 2, from which it is found that the proposed approach drastically reduce CO₂ and NO_x emissions.



(d) Time history of torque between the ICE and the EM driving conditions

Fig. 13 (continued)

4.4 Accuracy of response surface

Finally, the accuracy of response surface is shown in Fig. 14, where the circles denote the sampling points. The error is also summarized in Table 3. It is found from Fig. 14 and Table 3 that the highly accurate response surface is obtained and the error is much small. Therefore, it is considered that the pareto-frontier shown in Fig. 10 is reliable.

5 Conclusions

In this paper, a torque control strategy to reduce CO₂ and NO_x emissions for parallel HEV is developed. In ICE dominated HEV, it is important to develop a well-organized EMS taking into account the following driving conditions: (1) EM driving, (2) ICE driving, and (3) ICE driving assisted by EM. In the proposed torque control strategy, the ICE torque control function based on the BSFC map is introduced. This ICE torque control function consists of seven design variables. Simulation of the HEV is so computationally intensive that SAO using the RBF network is adopted to determine the ICE torque control function. In addition, the pareto-frontier between CO₂ and NO_x emissions is identified. Three representative driving cycles are used to examine the validity of the proposed approach. The trade-off is observed between CO₂ and NO_x, and these are effectively reduced. The validity of the proposed torque control strategy coupled with optimization is confirmed.

Appendix sequential approximate optimization with radial basis function network

A.1 Radial basis function network and width in the gaussian kernel

The RBF network is a three-layer feed-forward network. Given the training data expressed by $\{\mathbf{x}_j, y_j\} (j=1, 2, \dots, m)$, where m represents the number of sampling points, the output of the network \hat{y} (response surface) is given by

$$\hat{y}(\mathbf{x}) = \sum_{j=1}^m w_j K(\mathbf{x}, \mathbf{x}_j) \quad (\text{A1})$$

where m denotes the number of sampling points, $K(\mathbf{x}, \mathbf{x}_j)$ is the j -th basis function, and w_j denotes the weight of the j -th basis function. The following Gaussian kernel is generally used as the basis function:

$$K(\mathbf{x}, \mathbf{x}_j) = \exp\left(-\frac{(\mathbf{x}-\mathbf{x}_j)^T(\mathbf{x}-\mathbf{x}_j)}{r_j^2}\right) \quad (\text{A2})$$

In (A2), \mathbf{x}_j represents the j -th sampling point, and r_j is the width of the j -th basis function. The response y_j is calculated at the sampling point \mathbf{x}_j . The learning of RBF network is usually accomplished by solving

$$E = \sum_{j=1}^m (y_j - \hat{y}(\mathbf{x}_j))^2 + \sum_{j=1}^m \lambda_j w_j^2 \rightarrow \min \quad (\text{A3})$$

where the second term is introduced for the purpose of the

Table 2 Improvement of CO₂ and NO_x

Driving cycle		NEDC	JC08	WLTC	
ICE driving only	CO ₂ [g/km]	116.4	120.3	117.6	
	NO _x [mg/km]	250.2	273.5	295.5	
Proposed approach	Reference point	NEDC-A	JC08-A	WLTC-A	WLTC-B
	CO ₂ [g/km]	83.65	83.29	94.46	95.76
	NO _x [mg/km]	102.4	109.2	198.1	193.2
Improvement	CO ₂ [%]	28.14	30.76	19.68	18.57
	NO _x [%]	59.07	60.07	32.96	34.62

regularization. It is recommended that λ_j in (A3) is sufficient small value (e.g., $\lambda_j = 1.0 \times 10^{-2}$). Thus, the learning of RBF network is equivalent to finding the weight vector w . The

necessary condition of (A3) result in the following equation.

$$w = (H^T H + \Lambda)^{-1} H^T y \quad (\text{A4})$$

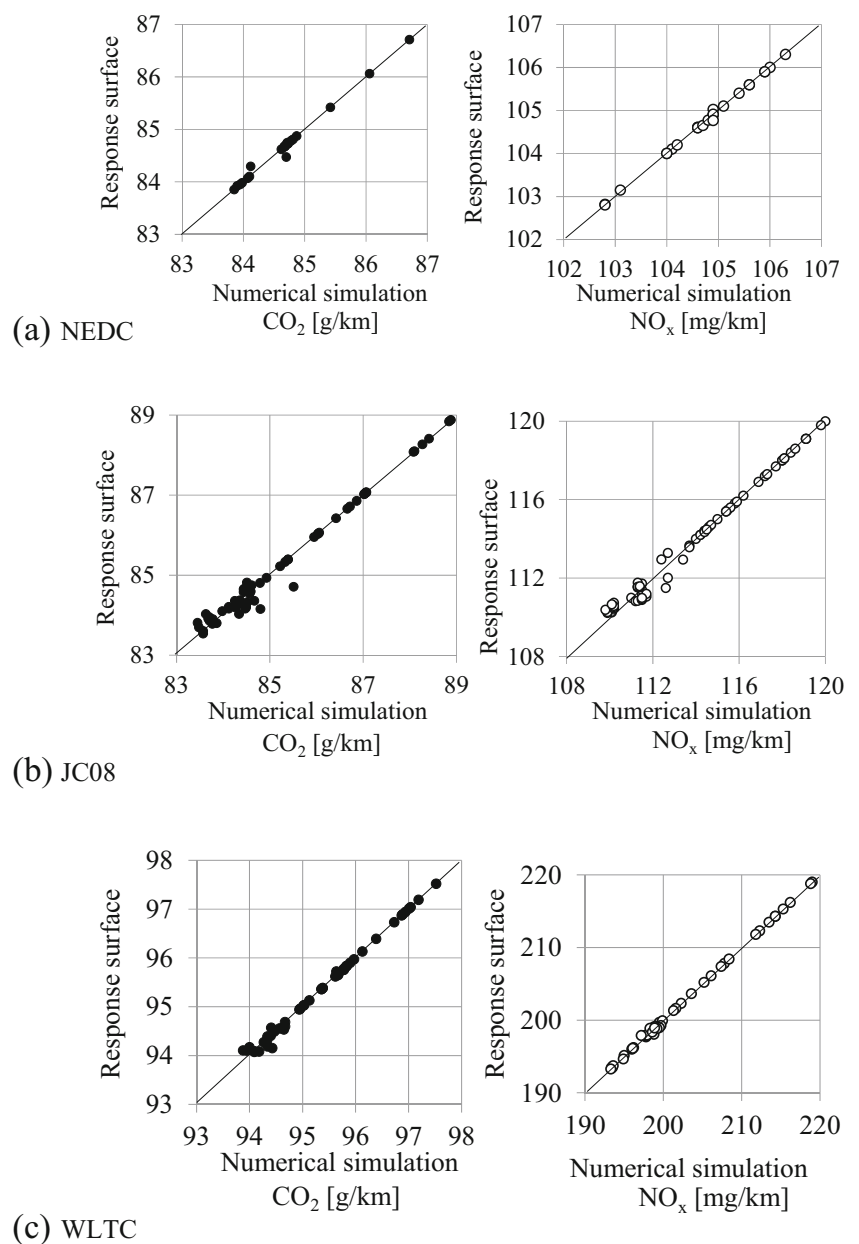
Fig. 14 Accuracy of response surface

Table 3 Error of each driving cycle

Driving cycle	Minimum [%]		Maximum [%]		Average [%]	
	CO2	NOx	CO2	NOx	CO2	NOx
NEDC	1.491E-04	9.332E-05	0.269	0.124	0.022	0.017
JC08	8.940E-05	4.959E-06	0.937	0.985	0.127	0.178
WLTC	4.693E-05	2.594E-04	0.295	0.389	0.038	0.060

where H , Λ and y are given as follows:

$$H = \begin{bmatrix} K(x_1, x_1) & K(x_1, x_2) & \cdots & K(x_1, x_m) \\ K(x_2, x_1) & K(x_2, x_2) & \cdots & K(x_2, x_m) \\ \vdots & \vdots & \ddots & \vdots \\ K(x_m, x_1) & K(x_m, x_2) & \cdots & K(x_m, x_m) \end{bmatrix}, \quad (A5)$$

$$\Lambda = \begin{bmatrix} \lambda_1 & 0 & \cdots & 0 \\ 0 & \lambda_2 & \cdots & 0 \\ \vdots & \vdots & \ddots & \vdots \\ 0 & 0 & 0 & \lambda_m \end{bmatrix}$$

$$y = (y_1, y_2, \dots, y_m)^T \quad (A6)$$

It is clear from (A4) that the learning of RBF network is equivalent to the matrix inversion $(H^T H + \Lambda)^{-1}$. The new sampling points are added through the SAO process. Using the RBF network, it is easy to calculate the weight vector w , because the additional learning is reduced to the incremental calculation of the matrix inversion.

The width in the Gaussian kernel plays an important role for good approximation. The first author of this paper has proposed the following simple estimate of the width (Kitayama et al. 2011):

$$r_j = \frac{d_{j,\max}}{\sqrt{n} \sqrt{m-1}} \quad j = 1, 2, \dots, m \quad (A7)$$

where r_j denotes the width of the j -th Gaussian kernel, and d_j ,

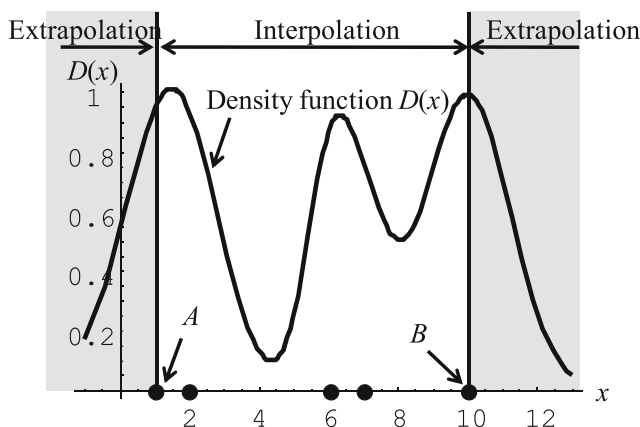


Fig. 15 Illustrative example of density function

$d_{j,\max}$ denotes the maximum distance between the j -th sampling point and the other sampling points. (A7) is applied to each Gaussian kernel individually, and can deal with the non-uniform distribution of sampling points.

A.2 Density function using RBF network

In the SAO, it is important to find out the unexplored region for global approximation. The Kriging can achieve this objective with the expected improvement (EI) function. In order to find out the unexplored region with the RBF network, we have developed a function called the density function (Kitayama et al. 2011). The basic idea is very simple. The local maxima are generated at the sampling points. To achieve this objective, every output y of the RBF network is replaced with +1. The procedure to construct the density function is summarized as follows:

(D-STEP1) The following vector y^D is prepared at the sampling points.

$$y^D = (1, 1, \dots, 1)_{m \times 1}^T \quad (A8)$$

(D-STEP2) The weight vector w^D of the density function $D(x)$ is calculated as follows:

$$w^D = (H^T H + \Lambda)^{-1} H^T y^D \quad (A9)$$

(D-STEP3) The density function $D(x)$ is minimized.

$$D(x) = \sum_{j=1}^m w_j^D K(x, x_j) \rightarrow \min \quad (A10)$$

(D-STEP4) The point minimizing $D(x)$ is taken as the new sampling point.

Figure 15 shows an illustrative example in one dimension. The black dots denote the sampling points. It is found from Fig. 5 that local minima are generated around the unexplored region. The RBF network is basically the interpolation between sampling points: therefore, points A and B in Fig. 15 are the lower and upper bounds of the design variables of the density function.

References

- Baumann BM, Washington G, Glenn BC, Rizzoni G (2000) Mechatronics design and control of hybrid electric vehicles. *IEEE/ASME Trans Mechatron* 5(1):58–72
- Chau KT, Wong YS (2002) Overview of power management in hybrid electric vehicle. *Energy Convers Manag* 43:1953–1968
- Delprat S, Lauber J, Guerra TM, Rimaux J (2004) Control of a parallel hybrid powertrain: optimal control. *IEEE Trans Veh Technol* 53(3):872–881
- Donald J, Schonlau M, Welch WJ (1998) Efficient global optimization of expensive black-box functions. *J Glob Optim* 13:455–492
- Guemri M, Neffati A, Caux S, Ngueveu SU (2014) Management of distributed power in hybrid vehicles based on D.P. or Fuzzy logic. *Optim Eng* 15(4):993–1012
- Hui S, Ji-hai J, Xin W (2009) Torque control strategy for a parallel hydraulic hybrid vehicle. *J Terramech* 46:259–265
- Kheir NA, Salman MA, Schouten NJ (2004) Emissions and fuel economy trade-off for hybrid vehicles using fuzzy logic. *Math Comput Simul* 66:155–172
- Kitayama S, Arakawa M, Yamazaki K (2011) Sequential approximate optimization using radial basis function network for engineering optimization. *Optim Eng* 12(4):535–557
- Kitayama S, Srirat J, Arakawa M, Yamazaki K (2013) Sequential approximate multi-objective optimization using radial basis function network. *Struct Multidiscip Optim* 48(3):501–515
- Koot M, Kesseks JTBA (2005) Energy management strategies for vehicular electric power systems. *IEEE Trans on Veh Technol* 54(3):771–782
- Kum D, Peng H, Bucknor NK (2011) Supervisory control of parallel hybrid electric vehicles for fuel emission reduction. *Trans ASME, J Dyn Syst, Meas, Control* 133:061010-1–061010-10
- Lin CC, Peng H, Grizzle JW (2003) Power management strategy for a parallel hybrid electric truck. *IEEE Trans Control Syst Technol* 11(6):839–849
- Long VT, Nhan NV (2012) Bee-algorithm-based optimization of component size and control strategy parameters for parallel hybrid electric vehicle. *Int J Automot Technol* 13(7):1177–1183
- Miettinen, K.M. (1998) *Nonlinear Multiobjective Optimization*, Kluwer Academic Publishers
- Montazeri-Gh M, Poursamad A, Ghalichi B (2006) Application of genetic algorithm for optimization of control strategy in parallel hybrid electric vehicle. *J Frankl Inst* 343:420–435
- Pei D, Leamy MJ (2013) Dynamic programming-informed equivalent cost minimization control strategy for hybrid-electric vehicle. *Trans ASME, J Dyn Syst Meas Control* 135:051013-1–051013-12
- Perez LV, Bossio GR, Moitre D, Garcia GO (2006) Optimization of power management in an hybrid electric vehicle using dynamic programming. *Math Comput Simul* 73:244–254
- Schouten NJ, Salman MA, Kheir NA (2003) Energy management strategies for parallel hybrid vehicles using fuzzy logic. *Control Eng Pract* 11:171–177
- Sinoquet D, Rousseau G, Milhau Y (2011) Design optimization and optimal control for hybrid vehicles. *Optim Eng* 12:199–213
- Wang L, Zhang Y, Yin C, Zhang H, Wang C (2012) Hardware-in-the-loop simulation for the design and verification of the control system of a series-parallel hybrid electric city-bus. *Simul Model Pract Theory* 25:148–162
- Wu J, Zhang CH, Cui NX (2008) PSO algorithm-based parameter optimization for HEV powertrain and its control strategy. *Int J Automot Technol* 9(1):53–69
- Zhu Y, Chen Y, Wu Z, Wang A (2006) Optimization design of an energy management strategy for hybrid vehicle. *Int J Altern Propuls* 1(1):47–62